RSC Advances

PAPER

View Article Online
View Journal | View Issue

Cite this: *RSC Adv.*, 2016, **6**, 84722

Construction of a ternary hybrid of CdS nanoparticles loaded on mesoporous-TiO_2/RGO for the enhancement of photocatalytic activity†

Hongwei Tian,*[a] Chenxing Wan,[a] Weitao Zheng,*[ab] Xiaoying Hu,[c] Liang Qiao[c] and Xiaoyi Wang[d]

Received 21st June 2016
Accepted 22nd August 2016

DOI: 10.1039/c6ra16094h

www.rsc.org/advances

We successfully fabricated a ternary hybrid of meso-TiO_2/RGO/CdS *via* an efficient electrostatic self-assembly approach and photo-assisted treatment. In the illumination process, GO nanosheets were reduced to RGO and simultaneously, CdS nanoparticles were uniformly loaded onto the surface of the meso-TiO_2/RGO. Compared with bare meso-TiO_2 (unitary component) and meso-TiO_2/RGO (binary components), the ternary meso-TiO_2/RGO/CdS exhibited superior photocatalytic activity and stability. In the experiment of the degradation of methylene orange (MO) in the presence of simulated solar light, the ternary hybrid showed the highest degradation rate (0.0228 min^{-1}), which was almost 2 and 17 times the degradation rate of meso-TiO_2/RGO and meso-TiO_2, respectively. This enhanced photoactivity is ascribed to the synergistic effect of meso-TiO_2, RGO and CdS, including a relatively high surface area, extension of the absorption spectrum range and the highly efficient separation and transfer rate of the charge carriers. The establishment of a ternary hybrid thus provides a promising way to improve the performance of photocatalysts.

1. Introduction

Mesoporous materials are of great interest regarding addressing the global energy shortage and environmental pollution.[1] Mesoporous materials possess a regular porous structure and controllable framework composition. Among these materials, mesoporous titania has attracted significant attention because of the fascinating advantages it offers, such as low cost, environmental friendliness, outstanding chemical stability, large specific surface area and great optical and electrical properties.[2–4] Designed to make use of visible light and to improve charge separation and transport, a lot of effort has been focused on elaborating a good design of TiO_2, including combining it with sensitizing agents, non-metal-doping, noble metal-doping, or with narrow-bandgap semiconductor materials.[5–8] Graphene–titania hybrid materials have generated extensive interest as a kind of emerging photocatalyst.[9–13]

Graphene has a high specific surface area and extremely low resistivity;[14–16] consequently, it has been coupled with mesoporous titania to enhance the catalytic performance. For example, Du *et al.* produced titania/graphene films with a hierarchically ordered macro–mesoporous structure showing efficient charge separation and the apparent rate constant increased to 0.071 min^{-1} from 0.045 min^{-1} with and without graphene.[17] Liu *et al.* indicated that TiO_2–graphene nanocomposites displayed improved adsorption capacity and photocatalytic selectivity for MO and MB.[18] Zhou *et al.* reported mesoporous anatase phase TiO_2 equipped with reduced graphene oxide, and this material exhibited a degradation rate of more than 4.5 times that of pure TiO_2 nanoparticles.[19]

However, in these cases, most graphene–mesoporous titania composites still degrade organic pollutants under UV light irradiation; therefore, the utilization of solar energy is quite insufficient for this purpose. Recently, Hayashi *et al.* reported an organic/inorganic ternary composite material, of which the IPCE value of FTO/SnO_2/(RGO + ZnONP + ZnP)$_m$ electrode reached 70%, which was much higher than the FTO/SnO_2/(ZnONP + ZnP)$_m$ electrode, with the generation of such a high photocurrent attributed to a hierarchical electron transfer cascade system.[20] Iwase *et al.* demonstrated that RGO, as an electron mediator (the third compound), can improve the water-splitting ability of the original binary photocatalytic ($BiVO_4$–Ru/$SrTiO_3$:Rh), and that the Z-scheme texture of RGO/$BiVO_4$ with

[a]*Department of Materials Science, Key Laboratory of Automobile Materials of MOE, Jilin University, Changchun, China. E-mail: tianhw@jlu.edu.cn; wtzheng@jlu.edu.cn*
[b]*State Key Laboratory of Automotive Simulation and Control, Jilin University, Changchun, China*
[c]*College of Science, Changchun University, Changchun, China*
[d]*Key Laboratory of Optical System Advanced Manufacturing Technology, Changchun Institute of Optics, Fine Mechanics and Physics, Chinese Academy of Sciences, Changchun, 130033, China*

† Electronic supplementary information (ESI) available: AFM for GO, photodegradation of the MO for TiO_2/RGO-*x*, TOC removal of the MO for meso-TiO_2, meso-TiO_2/RGO and meso-TiO_2/RGO/CdS, proposed mechanism diagram under visible light. See DOI: 10.1039/c6ra16094h

Ru/$SrTiO_3$:Rh facilitated electron–hole separation and transference.[21] Since that, the establishment of ternary structures has turned into an effective strategy to enhance the absorbing of solar light and photocatalytic capacity. Xu's group synthesized ternary hybrids of (reduced graphene oxide)–(CdS nanowire)–TiO_2 nanocomposites (CTG). Compared to the curly rGO–CdS nanowire, CTG extended the range of light-absorption and enhanced the electrical conductivity.[22] Liu and co-workers employed a two-step hydrothermal method to synthesize graphene/Fe^{3+}-doped TiO_2 nanowire composites, and found that the GR/Fe-NWCs showed the highest photocatalytic activity under visible light among the tested photocatalysts.[23] Yang *et al.* successfully obtained a novel ternary plasmonic heterojunction photocatalyst, and due to the strong visible-light response of Ag–AgBr/TiO_2, the RhB solution was completely degraded in 9 min.[24] To date, more similar ternary structures have emerged along with the higher demand for the photocatalytic capability of materials, *e.g.*, TiO_2/$InVO_4$/RGO,[25] TiO_2 nanotube–graphene–CdS quantum dots,[26] In_2O_3/CeO_2–TiO_2 [27] and C, N co-doping mesoporous Au/TiO_2.[28] Among these developing materials, cadmium sulfide (CdS) as a narrow band gap semiconductor is a good candidate and can absorb visible light and make composites it is part of exhibit excellent photocatalytic activity in the presence of visible light.[16,29–31]

The common means of obtaining ternary materials is *via* the assembly of various experimental methods, such as making use of UV-assisted treatment with successive ionic layer adsorption and reaction (SILAR) to synthesize TiO_2/RGO/Cu_2O,[32] sol–gel with solution-mixing for Ga-doped RGO/TiO_2,[33] electrostatic self-assembly with hydrothermal treatment for graphene–(CdS nanowire)–TiO_2 [22] and electrochemical reduction with SILAR to get TiO_2 nanotube–graphene–CdS quantum dots.[26] Besides, there are some reports that the reduction of GO to RGO has been completed by a UV-assisted treatment,[10,34] while others have adopted the illumination process to deposit CdS.[33,35] However, all of these involve two steps or separate operations. Herein, we utilize a one-step photo-assisted treatment to achieve simultaneously the reduction of GO and the deposition of CdS.

In our work, the ternary meso-TiO_2/RGO/CdS hybrid was fabricated first *via* an electrostatic self-assembly method to obtain meso-TiO_2/GO, followed by photo-assisted treatment to reduce GO and simultaneously deposit CdS. Compared with bare meso-TiO_2 and meso-TiO_2/RGO, the ternary meso-TiO_2/RGO/CdS exhibited superior photocatalytic performance for the degradation of MO under the irradiation of simulated solar light, and the degradation rate reached 0.0228 min^{-1}, which was almost 2 times and 17 times the degradation rates of meso-TiO_2/RGO and meso-TiO_2. The enhancement of the photocatalytic activity could be ascribed to the large specific surface area, the extensive photoresponse regions, and the highly efficient separation and transmission of the photo-induced charge carriers.

2. Experimental section

2.1 Material

Pluronic@F-127 (EO96PO70EO96, MW = 12 000 g mol^{-1}) was purchased from Sigma-Aldrich (USA). Tetrabutyl titanate ($Ti(OBu)_4$), acetic acid ($C_2H_4O_2$), hydrogen peroxide (H_2O_2, 30%), cadmium nitrate tetrahydrate ($Cd(NO_3)_2 \cdot 4H_2O$) and 3-aminopropyl-trimethoxysilane (APTES) were supplied by Sinopharm (Shanghai, China). Nitric acid (HNO_3), sulfuric acid (H_2SO_4), hydrochloric acid (HCl), sulfur sublimed (S) and ethanol (C_2H_6O) were obtained from Beijing Chemical Works (Beijing, China). Graphite powder was provided from Alfa Aesar China (Tianjin, China). All the materials were used without further purification. The deionized (DI) water used in these experiments was obtained from local sources.

2.2 Synthesis

2.2.1 Synthesis of graphene oxide (GO). Graphene oxide (GO) was produced from natural graphite fakes by a modified Hummers method.[36–38] In a typical experiment, 1 g graphite powder and 1 g $NaNO_3$ were added to 33 mL concentrated H_2SO_4 in a 3 °C ice-bath. Then, 6 g ground $KMnO_4$ was slowly added while stirring. Then, the mixture was stirred for 1.5 h at 35 °C, with slowly adding 40 mL distilled water to the mixture. The obtained mixture was stirred for a further 35 min at 90 °C. In the end, 100 mL distilled water was added to the mixture and 30 wt% H_2O_2 dropped gradually into it until the mixture turned bright yellow. Then, the mixture was washed with 150 mL 5% aqueous HCl to get rid of the metal ions, followed by washing with distilled water to effectively remove any remaining metal ions and acids. Finally, the resultant mixture was put into a vacuum drying oven at 60 °C. After 24 h, the brown exfoliated graphite oxide was obtained.

2.2.2 Synthesis of mesoporous TiO_2. Mesoporous TiO_2 was obtained *via* the template method based on Fan's work with modifications.[39] In a typical sol–gel process, 1.6 g of F127 was dissolved in 30 mL of ethanol by stirring for 30 min, and then stepwise was added 2.3 mL HOAc, 1.8 mL HNO_3 and 3.4 mL TBOT. The mixed solution was stirred continuously for 1 h and then poured into a 120 mm Petri dish. Then, the Petri dish was placed in an oven at 40 °C for 12 h to form a transparent membrane, followed by ageing at 65 °C for 24 h. Finally, the as-prepared membranes were calcined at 350 °C in an air atmosphere for 5 h (heating rate 2 °C min^{-1}) to eventually obtain mesoporous TiO_2.

2.2.3 Synthesis of meso-TiO_2/RGO and meso-TiO_2/RGO/CdS composites. The meso-TiO_2/RGO/CdS composite was prepared by a photo-assisted reduction and deposition method.[34,35] Typically, 0.1 g meso-TiO_2 was dispersed into 20 mL ethanol. Then, 1 mL of 3-aminopropyl-trimethoxysilane (APTES) was added, and the suspension was refluxed at 80 °C for 4 h. Subsequently, washing it three times with ethanol. Afterwards, the APTES-modified TiO_2 was added into 5.26 mg GO suspension after ultrasonication with stirring for 30 min to obtain a meso-TiO_2/GO suspension. The as-obtained meso-TiO_2/GO suspension, $Cd(NO_3)_2 \cdot 4H_2O$ and sublimed sulfur (S) were dispersed in ethanol and transferred to a glass reactor. Subsequently, the glass reactor containing the suspension kept at room temperature was exposed to the simulated solar light for 2 h. And then, the grey-green suspension was rinsed with ethanol and water a few times. Finally, the resultant was dried at 60 °C

overnight. Similarly, meso-TiO_2/RGO was synthesized by a photo-reduction in which meso-TiO_2/GO suspension was dispersed in ethanol and the above steps were repeated. Finally, we obtained the meso-TiO_2/RGO-x and meso-TiO_2/RGO/CdS, where x indicates the mass ratio of RGO dopant to meso-TiO_2.

2.3 Characterization

The as-obtained catalysts were examined with an X-ray diffractometer (XRD, a Bruker D8) with Cu K_α radiation. A Raman spectrometer (T64000 Horiba) was employed at a working power of 5 mW, an accumulation time of 30 s, and an excitation wavelength of 514.5 nm. X-ray photoelectron spectroscopy (XPS) measurements were conducted on a Thermo ESCALAB 250 spectrometer with a hemisphere detector at an energy resolution of 0.1 eV offered by an Al K_α radiation source. Fourier transform infrared spectra (FT-IR) were collected by a Biorad FTS-60A equipped with a diffuse reflectance unit. Transmission electron microscopy (TEM) and high-resolution transmission electron microscopy (HRTEM) images were obtained by a JEOL model JEM-2100F instrument operated at 200 kV. The Brunauer–Emmett–Teller (BET) specific surface areas of the sample powders were obtained through nitrogen adsorption–desorption, measured on an ASAP 2020 micromeritics surface and porosity analyser (USA). Ultraviolet-visible (UV-vis) absorption spectra were surveyed using a UV-vis spectrometer (UV-2500, Shimadzu, Japan), in which $BaSO_4$ was chosen as the reference standard. The electrochemical analysis was investigated by a conventional three-electrode system measured on CHI660E. The sample dispension on the clean fluorine-doped tin oxide (FTO) glass was used on the working electrode, and the immersed area of FTO was 0.8 cm^2. Also, the Ag/AgCl electrode and Pt electrode were chosen as the reference electrode and counter electrode, respectively. The photocurrent measurements were performed in three electrode quartz cells. The electrolyte was 0.2 M aqueous Na_2SO_4 solution (pH = 6.8) without additives. The light was emitted by a Xe arc lamp at a power of 300 W (PLS-SXE 300, Beijing Perfectlight Co. Ltd., China).

2.4 Photocatalytic performance

The photocatalytic activities of the ternary composites were detected through the degradation of MO operated by a 300 W Xe arc lamp equipped without a filter ($300 < \lambda < 800$ nm) for simulated solar light and with a cut-off filter ($\lambda > 400$ nm) for visible light, respectively. First, 20 mg samples were dispersed in 60 mL of MO solution (10 mg L^{-1}). To reach an adsorption–desorption equilibrium, the suspension was stirred in the dark for 30 min. During the photocatalytic reaction, 4 mL of the sample solution was extracted every other 30 min. Also, then the remaining photocatalysts were removed by centrifugation at 8000 rpm. Afterwards, the solution was analysed by a UV-vis spectrophotometer to determine the concentration of MO through observing the 464 nm absorption peak. The degradation ratio was defined as $(C_0 - C)/C_0$, where C refers to the absorption of dye in solution at a certain moment and C_0 refers to the absorption of the initial concentration at each time point.

3. Result and discussion

The XRD patterns of meso-TiO_2, meso-TiO_2/RGO, and meso-TiO_2/RGO/CdS are revealed in Fig. 1. This shows that the as-prepared meso-TiO_2 has a typical anatase framework according to JCPDS no. 21-1272. The meso-TiO_2/RGO presents the same diffraction peaks as the bare meso-TiO_2. After loading the CdS nanoparticles, some additional peaks appear at 26.9° and 43.9°, which might be due to the photo-assisted process to obtain the highly disperse and low-content CdS nanoparticles. In addition, the diffraction peaks of GO arise at approximately 10° and 43°, but no identical peaks are observed in meso-TiO_2/RGO and meso-TiO_2/RGO/CdS composites. This could be due to the low amount of graphene and the reduction of GO to RGO after illumination.

The Raman spectra of GO, meso-TiO_2/RGO and meso-TiO_2/RGO/CdS composites are shown in Fig. 2, from which we can observe the two typical Raman bands situated at 1354 cm^{-1} and

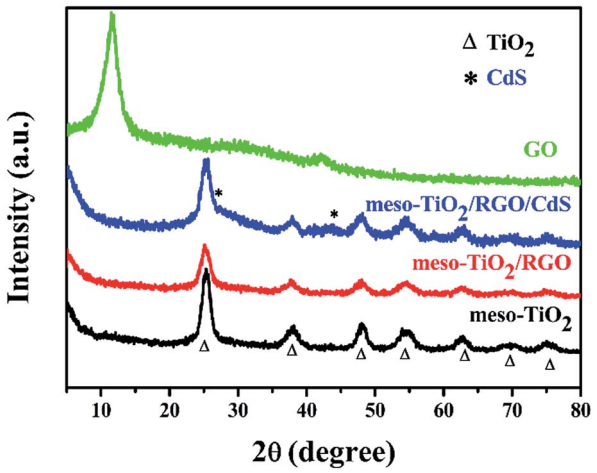

Fig. 1 XRD patterns of the GO, meso-TiO_2, meso-TiO_2/RGO, and meso-TiO_2/RGO/CdS samples.

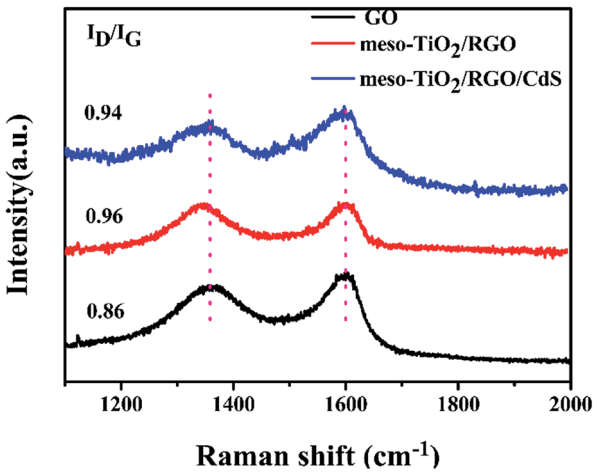

Fig. 2 Raman spectra of the GO, meso-TiO_2/RGO and meso-TiO_2/RGO/CdS samples.

1606 cm^{-1} corresponding to the sp^3 defects in graphene (D-band) and the sp^2 bonded carbon atoms (G-band), respectively.[40] After the photo-assisted reduction process, the positions of the D-band and G-band of meso-TiO_2/RGO and meso-TiO_2/RGO/CdS composites are basically unchanged. However, the intensity ratio between the D-band and G-band varies from 0.86 to 0.96 and 0.94, respectively, compared with GO nanosheets. This increasing ratio indicates the diminishment of the sp^2 domains' average size, suggesting that the illumination treatment achieved the deoxidation and reduction of GO.[4,41,42]

The fact that GO was reduced to RGO is also proved by the XPS results. The XPS patterns display a comparison of the C 1s peaks of GO, meso-TiO_2/RGO and meso-TiO_2/RGO/CdS composites, as shown in Fig. 3. The XPS spectrum in Fig. 3a highlights the abundance of diverse oxygen-containing functional groups, mainly including C–OH, C–O and O=C–O on the GO surface, corresponding to the peaks position at 286, 287.4 and 289.3 eV.[43] It is noteworthy the loss of the oxygen-containing functional groups in Fig. 3b and c of the meso-TiO_2/RGO and meso-TiO_2/RGO/CdS composites, which demonstrates the reduction of GO after light illumination.[22,44,45] Identically, the FT-IR spectra in Fig. 3d also indicate that the peaks of diverse oxygen-containing functional groups are obviously weakened after illumination treatment.

The morphology of the meso-TiO_2/RGO/CdS composite can be characterized by transmission electron microscopy (TEM). Fig. 4a shows that the disparate nanoparticles are united on monolayer or multilayer graphene nanosheets, as also proved by Fig. S1,† where the flocculence-aggregation can also be observed. Also, it can be clearly seen that TiO_2 nanocrystals with worm-like channels originating from the mesoporous structure are coated with wrinkled RGO nanosheets in Fig. 4b. The HRTEM image in Fig. 4c unambiguously shows that the specific interplanar spacings are 0.352 nm and 0.336 nm, respectively, belonging to the (101) facet of anatase TiO_2 and the (111) plane of a cubic phase CdS, which can be indicators to determine the

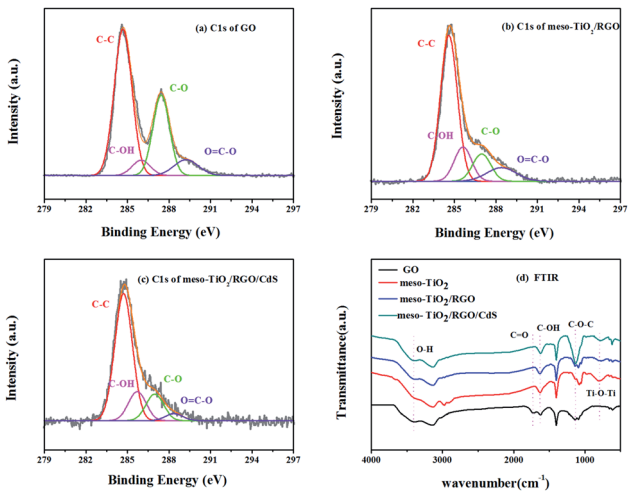

Fig. 3 XPS spectra of C 1s for GO (a), meso-TiO_2/RGO (b), and meso-TiO_2/RGO/CdS (c); Fourier transformed infrared spectra (FT-IR) of GO, meso-TiO_2 and meso-TiO_2/RGO, meso-TiO_2/RGO/CdS (d).

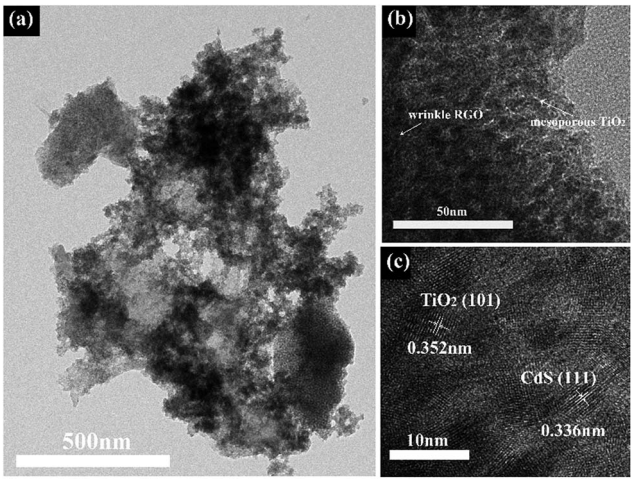

Fig. 4 The TEM images (a and b), HRTEM image (c) for meso-TiO_2/RGO/CdS.

coexistence of TiO_2 and CdS. In addition, based on the selected region in Fig. 5a, we can see the different-colour elements in the mapping images for Cd, S, C, O and Ti elements in Fig. 5b–f, indicating that CdS nanoparticles were successfully deposited on the surface of meso-TiO_2/RGO after photo-assisted treatment.

The porous structure and BET surface area of the meso-TiO_2/RGO/CdS composite was investigated by the nitrogen adsorption–desorption method. Fig. 6 shows the nitrogen sorption isotherm and the corresponding pore size distribution curve for meso-TiO_2/RGO/CdS. The isotherm curve of meso-TiO_2/RGO/CdS composite presents the typical IV isotherm curve and H2-type hysteresis loop, derived from the mesoporous material with ink-bottle channels. The BET surface area, pore volume and pore size of the ternary material, obtained from the isotherm, were calculated to be 117.73 $m^2 g^{-1}$, 0.19 $cm^3 g^{-1}$ and 6.55 nm, respectively. At this point, the porous structure and large surface area would be in favour of the photocatalytic performance of the meso-TiO_2/RGO/CdS composite.

UV-vis diffuse reflectance spectroscopy was used as a powerful instrument to determine the optical properties of meso-TiO_2, meso-TiO_2/RGO and meso-TiO_2/RGO/CdS, as shown in Fig. 7. It turns out that meso-TiO_2 absorbs only UV light, which relates to its wide band gap (*ca.* 3.2 eV). In contrast, meso-TiO_2/RGO shows better visible-light absorption, which indicates that the contribution of RGO should not be ignored. The absorption edge of meso-TiO_2/RGO/CdS exhibits an obvious red shift and the absorption range is extended to the visible-light district because of the deposition of CdS nanoparticles. CdS nanoparticles can adjust the electronic and optical properties of the prior composites.[26,46] The admirable light-absorbing ability of the ternary hybrid makes it a prospective material for solar-driven applications.

The photocatalytic performance of meso-TiO_2, meso-TiO_2/RGO and meso-TiO_2/RGO/CdS in aqueous contaminants was detected by the decomposition of MO dyes. In binary material, as shown in Fig. S2,† the optimum dopant weight is 5 wt%, therefore, we chose meso-TiO_2/RGO-5 as the control to prepare

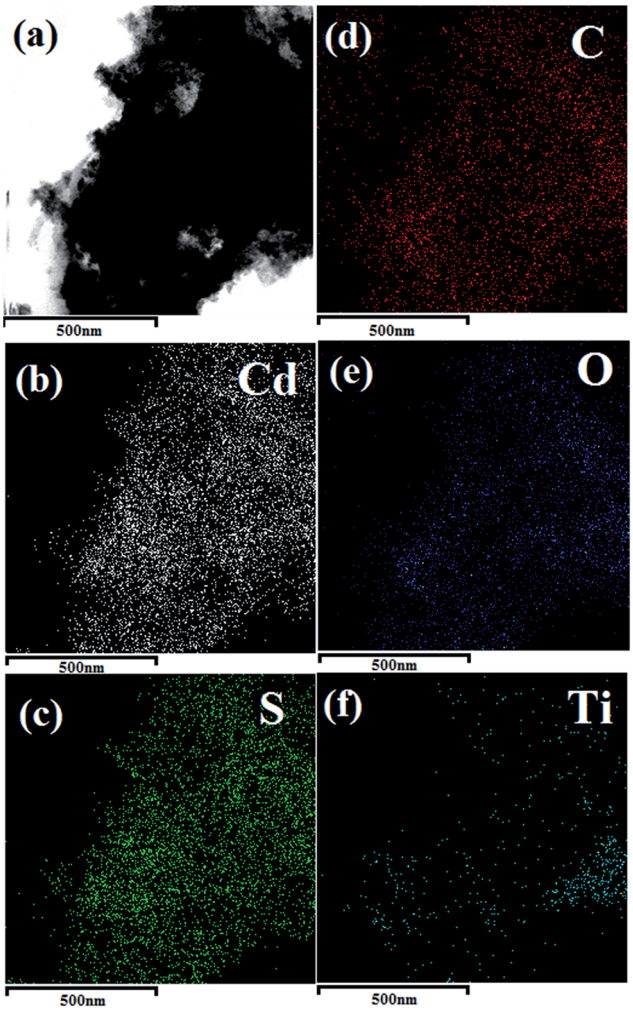

Fig. 5 The elemental mapping patterns ((b)–(f)) of the selected area (a) for meso-TiO_2/RGO/CdS.

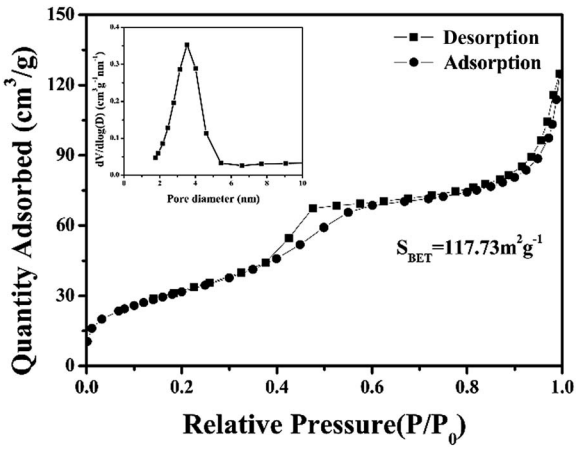

Fig. 6 Nitrogen sorption isotherm and the corresponding pore size distribution curve for meso-TiO_2/RGO/CdS.

the ternary hybrid. As shown in Fig. 8a, under the condition of simulated solar light, there is a feeble degradation of meso-TiO_2; whereas, by contrast, meso-TiO_2/RGO has a heightened

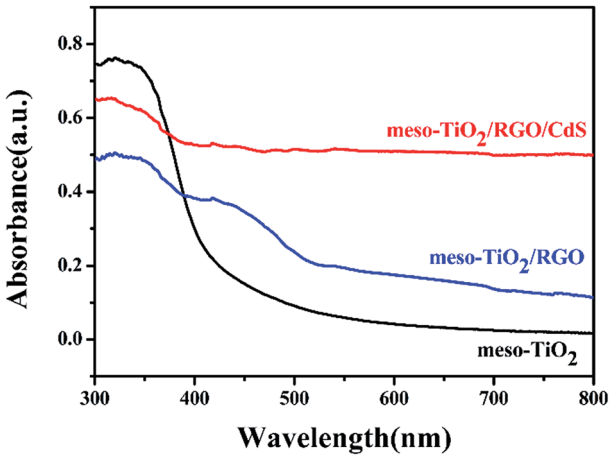

Fig. 7 UV-vis diffuse reflectance spectra for meso-TiO_2, meso-TiO_2/RGO and meso-TiO_2/RGO/CdS.

photocatalytic activity to a certain extent and meso-TiO_2/RGO/CdS presents the prominently highest photoactivity, whereby when the illumination time is 120 min, the degradation rate reaches 94% and the apparent reaction rate constant of the ternary material in Fig. 8c is 0.0228 min^{-1}, which is almost 2 and 17 times the degradation rate of meso-TiO_2/RGO and meso-TiO_2, respectively. Moreover, Fig. 8b presents the photodegradation activity of the three samples treated with visible light. The bare meso-TiO_2 is basically ineffective and the impact of meso-TiO_2/RGO is also quite weak, but meso-TiO_2/RGO/CdS exhibits a growing photocatalytic capability. Combined with Fig. 8a–c, it is facile to infer that the introduction of graphene and the loading of CdS can greatly strengthen the photocatalytic activity, and that is why the ternary meso-TiO_2/RGO/CdS catalyst shows the best performance under the condition of visible light.

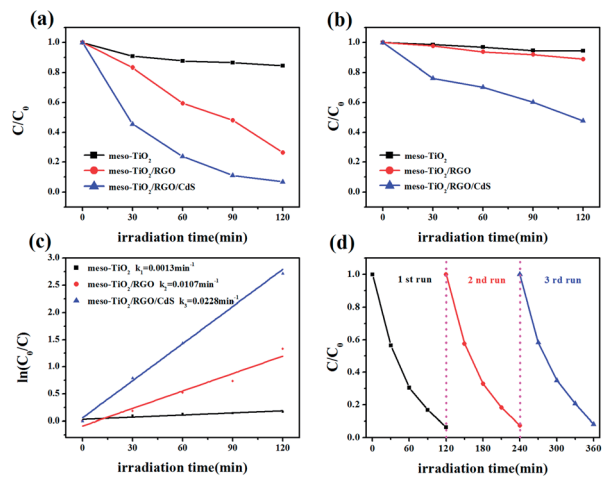

Fig. 8 Photodegradation of MO in the presence of the simulated solar light (a), visible light (b) of meso-TiO_2, meso-TiO_2/RGO and meso-TiO_2/RGO/CdS; the apparent reaction rate constants k of meso-TiO_2, meso-TiO_2/RGO and meso-TiO_2/RGO/CdS (c) and the recycling runs of meso-TiO_2/RGO/CdS for degrading MO (d) under simulated solar light.

For the stability of the ternary photocatalyst, as shown in Fig. 8d, the degradation efficiency shows a slight decrease at almost 91% after three recycling runs in the photodegradation of MO irradiated by simulated solar light. This result indicates that meso-TiO_2/RGO/CdS has the highest stability and an excellent photocatalytic capacity, and hence it could be regarded as a kind of reusable resource applied to pollutant degradation and other fields.

In light of the above results, one can attribute the boosted photocatalytic performance of the ternary hybrid in the MO's decomposition to the following three factors: (1) the graphene nanosheets that cover meso-TiO_2 nanocrystals not only provide more active sites for the degradation reaction, but also effectively accelerate the separation efficiency of carriers;[32] (2) meso-TiO_2/RGO/CdS can absorb in the visible-light region of the solar spectrum owing to the decoration of CdS nanoparticles; (3) there is potential and inseparable synergy among meso-TiO_2, RGO and CdS that can facilitate the charge transfer and separation in the meso-TiO_2/RGO/CdS composite.[22,26]

For attesting to the favourable effect of the graphene nanosheets and CdS nanoparticles in meso-TiO_2/RGO/CdS toward the light harvesting and transfer of photoexcited electron–hole pairs, photoelectrochemical analysis was performed on the meso-TiO_2, meso-TiO_2/RGO and meso-TiO_2/RGO/CdS treated with simulated solar light. As pointed out in Fig. 9a, after several on–off cycles of regular irradiation of the simulated solar light, the transient photocurrent responses of meso-TiO_2, meso-TiO_2/RGO and meso-TiO_2/RGO/CdS photoelectrodes were still reproducible and stable. It is widely known that the diffusion of photoexcited electrons and the harvesting of photo-induced holes in the electrolyte can generate a photocurrent.[44] The meso-TiO_2/RGO/CdS photo-electrode had the markedly highest photocurrent responses compared to meso-TiO_2/RGO and bare meso-TiO_2, which hints at the more efficient transmission and the longer-time separation for the photogenerated carries.

The results of the experiment involving electrochemical impedance spectroscopy (EIS) irradiated with the simulated solar light are shown in Fig. 9b, from which we can see that meso-TiO_2/RGO and meso-TiO_2/RGO/CdS have smaller impedance arc radiuses compared to meso-TiO_2. Moreover, the impedance arc radius of meso-TiO_2/RGO/CdS is the smallest among these three samples, indicating that meso-TiO_2/RGO/CdS, with the best electrical conductivity, would best facilitate the migration of the photoexcited carriers, and therefore, the photocatalytic efficiency can be enhanced.

In light of the above results and analyses, we can offer a reasonable explanation for the enhanced photocatalytic capacity of meso-TiO_2/RGO/CdS, as illustrated in Fig. 10. In the presence of simulated solar light, CdS and TiO_2 simultaneously play a role in absorbing the simulated solar light. First, the electrons are excited from the valence band (VB) of both CdS and TiO_2 to the respective conduction band (CB). Second, because the E_{CB} of TiO_2 (−0.29 V *vs.* NHE) and CdS (−0.53 V *vs.* NHE)[35] are more negative than the standard redox potential of O_2/O_2^- (−0.28 V *vs.* NHE),[47] the photoexcited electrons with strong reductive ability can react with the dissolved oxygen molecule (O_2) to obtain superoxide radicals (O_2^-). In addition, the RGO nanosheets not only provide a reaction zone, but also the electrons can transfer to the RGO nanosheets from the CB of TiO_2 and CdS, resulting in the separation of electron–hole pairs due to the lower potential (−0.08 V *vs.* NHE)[47] than the E_{CB} of TiO_2 and CdS.

At the same time, H_2O and hydroxy (–OH) are absorbed by the rest of holes of TiO_2 to obtain the hydroxyl radicals (˙OH), while the E_{VB} of CdS (+1.88 V *vs.* NHE) is not so positive that the holes of CdS cannot react with H_2O and –OH, but the holes themselves have strong oxidizability and can directly oxidize dyes into CO_2 and H_2O. Therefore, the superoxide radicals, holes and hydroxyl radicals can participate in the reaction to achieve the degradation.

On the other side, in the presence of visible light, Fig. S3† reflects that CdS plays the major role, in which the electrons are excited from the VB to the CB and the holes are then left in the VB. The electrons, besides the above transfer paths, can also transfer to the CB of TiO_2. The remaining reaction processes are similar to the above-mentioned processes.

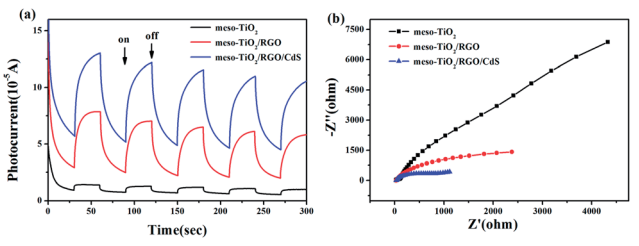

Fig. 9 Transient photocurrent response (a) and electrochemical impedance spectroscopy (EIS) Nyquist plots (b) of the sample electrodes of the bare meso-TiO_2, meso-TiO_2/RGO and meso-TiO_2/RGO/CdS treated with simulated solar light (300 < λ < 800 nm).

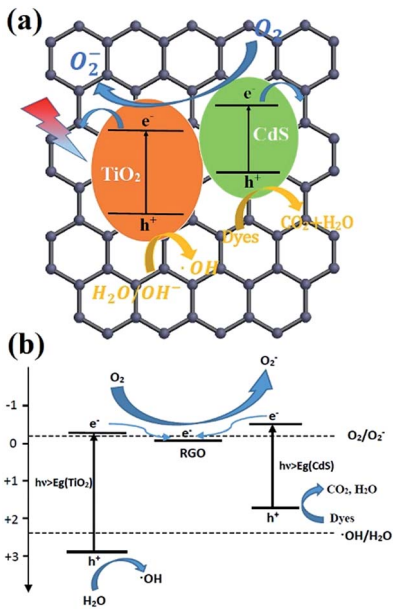

Fig. 10 Proposed mechanism diagram (a) and redox potential diagram (b) illustrating the photocatalytic redox reactions with the ternary meso-TiO_2/RGO/CdS catalyst in the presence of simulated solar light.

Whichever mechanism is used, TiO_2 with an ordered porous structure is the major catalyst for the photocatalytic decomposition of MO, while RGO as an electron capture device accelerates the transfer of photogenerated charges and offers more active sites and reaction and CdS nanoparticles serve as a catalyst promoter to effectively enhance the solar-light absorption. Each individual constituent acts synergistically in such a way that makes meso-TiO_2/RGO/CdS display an obviously higher photacatalytic activity over meso-TiO_2/RGO and meso-TiO_2.

4. Conclusion

Ternary meso-TiO_2/RGO/CdS hybrid materials were synthesized through an electrostatic self-assembly approach and a one-step photo-assisted reduction and deposition process. The ternary hybrids possess an ordered mesoporous structure, a relatively high surface area and a highly efficient separation and transfer rate of the photogenerated carriers. Most importantly, the ternary meso-TiO_2/RGO/CdS exhibited superior photocatalytic activity and stability. For the degradation of MO in the presence of simulated solar light, the degradation rate reached up to 0.0228 min^{-1}, which was almost 2 and 17 times the degradation rate of meso-TiO_2/RGO and meso-TiO_2, respectively. Based on our investigations, the enhanced photoactivity depends on the synergistic effect among the individual constituents of the catalyst, including RGO serving as an electron capture device to boost the transfer of the photoexcited charges and CdS nanoparticles also effectually enhancing the solar-light absorption. The above-discussed results demonstrate that the ternary hybrid is an alternative strategy to improve the photocatalytic performance of mesoporous TiO_2.

Acknowledgements

Financial supports from the NSF (No. 51472106, 51202017 and 51372095) of China and the NSF (No. 20140101107JC and 20140101092JC) of Jilin Province are highly appreciated.

Notes and references

1 M. E. Davis, *Nature*, 2002, **417**, 813–821.
2 H. G. Yang, C. H. Sun, S. Z. Qiao, J. Zou, G. Liu, S. C. Smith, H. M. Cheng and G. Q. Lu, *Nature*, 2008, **453**, 634–638.
3 X. L. Hu, G. S. Li and J. C. Yu, *Langmuir*, 2010, **26**, 3031–3039.
4 J. C. Liu, H. W. Bai, Y. J. Wang, Z. Y. Liu, X. W. Zhang and D. D. Sun, *Adv. Funct. Mater.*, 2010, **20**, 4175–4181.
5 G. Liu, L. Z. Wang, H. G. Yang, H. M. Cheng and G. Q. Lu, *J. Mater. Chem.*, 2010, **20**, 831–843.
6 J. G. Yu, T. T. Ma and S. W. Liu, *Phys. Chem. Chem. Phys.*, 2011, **13**, 3491–3501.
7 S. G. Kumar and L. G. Devi, *J. Phys. Chem. A*, 2011, **115**, 13211–13241.
8 C. Xue, X. Xu, G. D. Yang and S. J. Ding, *RSC Adv.*, 2015, **5**, 102228–102237.
9 L. Bai, F. Fang, Y. Y. Zhao, Y. G. Liu, J. P. Li, G. Y. Huang and H. Y. Sun, *RSC Adv.*, 2014, **4**, 43039–43046.
10 G. Williams, B. Seger and P. V. Kamat, *ACS Nano*, 2008, **2**, 1487–1491.
11 H. Zhang, X. J. Lv, Y. M. Li, Y. Wang and J. H. Li, *ACS Nano*, 2010, **4**, 380–386.
12 Y. Y. Liang, H. L. Wang, H. S. Casalongue, Z. Chen and H. J. Dai, *Nano Res.*, 2010, **3**, 701–705.
13 B. Lin, G. Yang, B. Yang and Y. Zhao, *Appl. Catal., B*, 2016, **198**, 276–285.
14 Q. J. Xiang, J. G. Yu and M. Jaroniec, *Chem. Soc. Rev.*, 2012, **41**, 782–796.
15 Q. J. Xiang, J. G. Yu and M. Jaroniec, *J. Phys. Chem. C*, 2011, **115**, 7355–7363.
16 Q. Li, B. D. Guo, J. G. Yu, J. R. Ran, B. H. Zhang, H. J. Yan and J. R. Gong, *J. Am. Chem. Soc.*, 2011, **133**, 10878–10884.
17 J. Du, X. Y. Lai, N. L. Yang, J. Zhai, D. Kisailus, F. B. Su, D. Wang and L. Jiang, *ACS Nano*, 2011, **5**, 590–596.
18 S. W. Liu, C. Liu, W. G. Wang, B. Cheng and J. G. Yu, *Nanoscale*, 2012, **4**, 3193–3200.
19 Q. Zhou, Y. H. Zhong, X. Chen, X. J. Huang and Y. C. Wu, *Mater. Res. Bull.*, 2014, **51**, 244–250.
20 H. Hayashi, I. V. Lightcap, M. Tsujimoto, M. Takano, T. Umeyama, P. V. Kamat and H. Imahori, *J. Am. Chem. Soc.*, 2011, **133**, 7684–7687.
21 A. Iwase, Y. H. Ng, Y. Ishiguro, A. Kudo and R. Amal, *J. Am. Chem. Soc.*, 2011, **133**, 11054–11057.
22 S. Q. Liu, M. Q. Yang and Y. J. Xu, *J. Mater. Chem. A*, 2014, **2**, 430–440.
23 W. Q. Li, X. Liu and H. X. Li, *J. Mater. Chem. A*, 2015, **3**, 15214–15224.
24 C. Xue, X. Yan, S. Ding and G. Yang, *RSC Adv.*, 2016, **6**, 68653–68662.
25 X. Lin, D. Xu, Z. Lin, S. S. Jiang and L. M. Chang, *RSC Adv.*, 2015, **5**, 84372–84380.
26 J. J. Xian, D. Z. Li, J. Chen, X. F. Li, M. He, Y. Shao, L. H. Yu and J. L. Fang, *ACS Appl. Mater. Interfaces*, 2014, **6**, 13157–13166.
27 M. Myilsamy, V. Murugesan and M. Mahalakshmi, *Appl. Catal., A*, 2015, **492**, 212–222.
28 L. Li, B. H. Wu, G. N. Li and Y. S. Li, *RSC Adv.*, 2016, **6**, 28904–28911.
29 X. Wang, G. Liu, Z. G. Chen, F. Li, L. Wang, G. Q. Lu and H. M. Cheng, *Chem. Commun.*, 2009, **23**, 3452–3454.
30 Y. Tak, S. J. Hong, J. S. Lee and K. Yong, *J. Mater. Chem.*, 2009, **19**, 5945–5951.
31 L. Wu, J. C. Yu and X. Z. Fu, *J. Mol. Catal. A: Chem.*, 2006, **244**, 25–32.
32 W. Q. Fan, X. Q. Yu, H. C. Lu, H. Y. Bai, C. Zhang and W. D. Shi, *Appl. Catal., B*, 2016, **181**, 7–15.
33 M. R. Hasan, S. B. Abd Hamid, W. J. Basirun, Z. Z. Chowdhury, A. E. Kandjani and S. K. Bhargava, *New J. Chem.*, 2015, **39**, 369–376.
34 X. Yan, Y. J. Li, F. Du, K. Zhu, Y. Q. Zhang, A. Y. Su, G. Chen and Y. J. Wei, *Nanoscale*, 2014, **6**, 4108–4116.
35 X. Y. Pan and Y. J. Xu, *J. Phys. Chem. C*, 2015, **119**, 7184–7194.
36 A. K. Geim, *Science*, 2009, **324**, 1530–1534.
37 S. Stankovich, D. A. Dikin, R. D. Piner, K. A. Kohlhaas, A. Kleinhammes, Y. Jia, Y. Wu, S. T. Nguyen and R. S. Ruoff, *Carbon*, 2007, **45**, 1558–1565.

38 Y. Zhu, S. Murali, W. Cai, X. Li, J. W. Suk, J. R. Potts and R. S. Ruoff, *Adv. Mater.*, 2010, **22**, 3906–3924.
39 J. Fan, S. W. Boettcher and G. D. Stucky, *Chem. Mater.*, 2006, **18**, 6391–6396.
40 Q. J. Xiang, J. G. Yu and M. Jaroniec, *Nanoscale*, 2011, **3**, 3670–3678.
41 Y. H. Ng, A. Iwase, A. Kudo and R. Amal, *J. Phys. Chem. Lett.*, 2010, **1**, 2607–2612.
42 L. Sun, Z. L. Zhao, Y. C. Zhou and L. Liu, *Nanoscale*, 2012, **4**, 613–620.
43 J. E. Benedetti, D. R. Bernardo, A. Morais, J. Bettini and A. F. Nogueira, *RSC Adv.*, 2015, **5**, 33914–33922.
44 Y. H. Zhang, Z. R. Tang, X. Fu and Y. J. Xu, *ACS Nano*, 2011, **5**, 7426–7435.
45 Y. H. Zhang, N. Zhang, Z. R. Tang and Y. J. Xu, *ACS Nano*, 2012, **6**, 9777–9789.
46 G. S. Li, D. Q. Zhang and J. C. Yu, *Environ. Sci. Technol.*, 2009, **43**, 7079–7085.
47 X. W. Wang, H. W. Tian, X. Q. Cui, W. T. Zheng and Y. C. Liu, *Dalton Trans.*, 2014, **43**, 12894–12903.